Solid-solution Er:(Sc,Y)2O3 transparent ceramics: Optical spectroscopy, inhomogeneous line broadening, C sites and mid-infrared laser operation

Simone Normani, Pavel Loiko, Roman Maksimov, Liza Basyrova, Vladislav Shitov, Elena Dunina, Alexey Kornienko, Liudmila Fomicheva, Alain Braud, Ammar Hideur, et al.

"Mixed" Er:$(Sc,Y)_2O_3$ transparent ceramics: Optical spectroscopy, inhomogeneous line broadening, C_{3i} sites and mid-infrared laser operation

Simone Normani[1], Pavel Loiko[1,*], Roman Maksimov[2,3], Liza Basyrova[1], Vladislav Shitov[3], Elena Dunina[4], Alexey Kornienko[4], Liudmila Fomicheva[5], Alain Braud[1], Ammar Hideur[6], Bruno Viana,[7] and Patrice Camy[1]

[1]Centre de Recherche sur les Ions, les Matériaux et la Photonique (CIMAP), UMR 6252 CEA-CNRS-ENSICAEN, Université de Caen Normandie, 6 Boulevard Maréchal Juin, 14050 Caen Cedex 4, France
[2]Ural Federal University named after the first President of Russia B.N. Yeltsin, 19 Mira St., 620002 Ekaterinburg, Russia
[3]Institute of Electrophysics, Ural Branch of the Russian Academy of Sciences, 106 Amundsen St., 620016 Ekaterinburg, Russia
[4]Vitebsk State Technological University, 72 Moskovskaya Ave., 210035, Vitebsk, Belarus
[5]Belarusian State University of Informatics and Radioelectronics, 6 Brovki St., 220027, Minsk, Belarus
[6]CORIA UMR 6614, CNRS-INSA-Université de Rouen, Normandie Université, Avenue de l'université, BP. 12, 76801 Saint Etienne du Rouvray, France
[7]Chimie ParisTech, PSL University, CNRS, Institut de Recherche de Chimie Paris, 11 rue Pierre et Marie Curie, 75005 Paris, France
**Corresponding author, e-mail: pavel.loiko@ensicaen.fr*

Abstract: Rare-earth-doped transparent sesquioxide laser ceramics enable engineering of their gain bandwidths via solid-solution ("mixed") compositions exhibiting a strong inhomogeneous spectral line broadening. We report on a detailed spectroscopic study and the first mid-infrared laser operation of Erbium-doped yttria-scandia, $(Sc_xY_{1-x})_2O_3$, ceramics fabricated by vacuum sintering at 1750 °C from laser-ablated nanoparticles. The effect of the Sc fraction on the spectral and kinetic properties of Er^{3+} emission around 2.8 μm owing to the $^4I_{11/2} \rightarrow {}^4I_{13/2}$ is revealed. The inhomogeneous spectral line broadening leading to merging of individual Stark sub-levels of Er^{3+} multiplets is evidenced by low-temperature spectroscopy. An original method of quantifying the distribution of dopant Er^{3+} ions over C_2 and C_{3i} symmetry sites in the cubic bixbyite structure is suggested based on the transition probabilities derived by the Judd-Ofelt theory. In the parent Er:Y_2O_3 ceramic, the Er^{3+} ions nearly follow the ideal distribution with 3/4 of ions residing in C_2 sites, and Sc addition skews it in favor of C_{3i} sites. A continuous-wave Er:$(Sc,Y)_2O_3$ ceramic laser generated 312 mW at 2716 nm with a slope efficiency of 18.6% and a laser threshold of 128 mW.

Keywords: transparent ceramics; sesquioxides; erbium ions; luminescence; mid-infrared lasers.

1. Introduction

Transparent ceramics are polycrystalline materials composed of randomly oriented closely packed single-crystalline grains featuring weak light scattering [1-3]. The latter can originate from pores, grain boundaries, impurities and birefringence effects [1]. When doped with trivalent rare-earth ions (RE^{3+}), transparent ceramics appear as appealing laser materials [3-5]. As compared to the corresponding single crystals, laser ceramics offer a number of advantages such as i) reduced synthesis temperatures [6,7], ii) easier control of RE^{3+} doping [8] and access to "mixed" (solid-solution) compositions $A_{1-x}B_x$ [9-11], iii) fabrication of composite elements [12,13] and iv) size-scalable production [14,15]. The advantageous spectroscopic and thermo-mechanical properties of crystalline materials are often well preserved for laser ceramics [16,17]. Usually, cubic materials are employed for fabricating transparent laser ceramics, notably garnets [18-20] and sesquioxides [21-23] (oxide matrices), as well as alkaline earth metal fluorides [24,25].

Cubic rare-earth sesquioxides with a chemical formula A_2O_3 (where A stands for Y, Lu, Sc, or their mixture), are attractive laser host crystals for RE^{3+} doping targeting the development of short-wave infrared lasers [26]. As host matrices, they feature good thermal and thermo-optical properties (namely, high thermal conductivity, 15.94 $Wm^{-1}K^{-1}$ for undoped Y_2O_3 determined by the laser flash method [27]), broadband transparency (0.22 – 8 μm for Y_2O_3), and low phonon energies (among oxide materials, 592 cm^{-1} for Y_2O_3). Cubic sesquioxides can accommodate RE^{3+} dopants in high concentrations [28] reaching the stoichiometric compositions [29]. The RE^{3+} ions in sesquioxide crystals experience very strong crystal fields leading to large Stark splitting of their manifolds [30]. The main drawback of A_2O_3 compounds is their high melting points (2430 °C for Y_2O_3 [31]) making the melt growth of large-sized and internal stress-free single crystals challenging [32,33]. As mentioned above, sesquioxides are well suited for transparent ceramic technology which can leverage the synthesis temperatures down to ~1400 °C [34]. RE^{3+}-doped transparent sesquioxide laser ceramics are widely known [21].

One of the advantages of ceramic technology is its flexibility for material engineering relying on compositionally "mixed" compounds [9,10,22]. It can be exploited for cubic sesquioxides due to a combination of two factors, namely i) the existence of substitution solid-solutions in the $xY_2O_3 - yLu_2O_3 - zSc_2O_3$ ternary system for the entire range of $x + y + z = 1$ [35], and ii) a strong sensitivity of the crystal-field strength to the nature of the host-forming cation [30]. The latter helps to induce a strong compositional disorder leading to a notable inhomogeneous spectral line broadening. Such a route towards engineering the gain bandwidth for laser-active RE^{3+} ions enables the development of "mixed" laser gain media supporting broadband tuning of laser emission and generation of femtosecond pulses from mode-locked lasers, as demonstrated for Tm^{3+}-doped "mixed" sesquioxide ceramics at ~2 μm [36-38].

Trivalent erbium ions (Er^{3+}) are known for their short-wave infrared (SWIR) emission at ~2.8 μm originating from the $^4I_{11/2} \rightarrow {}^4I_{13/2}$ electronic transition [39]. Due to the strong absorption of such radiation by water in biological tissues, ~2.8 μm lasers are relevant for applications in

medicine (laser surgery) enabling precise control of incisions. 2.8-μm lasers can also be used for frequency down-conversion in mid-infrared coherent sources, such as Fe^{2+}-based lasers, optical parametric oscillators and supercontinuum sources. Cubic sesquioxide crystals and transparent polycrystalline ceramics are attractive for Er^{3+} doping, with the aim of 2.8-μm laser development [39-41]. First, due to the low phonon energy spectrum of A_2O_3 compounds, the rate of multiphoton non-radiative relaxation from the upper laser level ($^4I_{11/2}$) is reduced [42]. Second, high rare-earth ion densities inherent to cubic sesquioxides boost the energy-transfer upconversion (ETU) between Er^{3+} ions ($^4I_{13/2} + {}^4I_{13/2} \rightarrow {}^4I_{9/2} + {}^4I_{15/2}$) recirculating the electronic population in favor of the upper laser level, which is of primary importance for avoiding the bottleneck effect for 2.8-μm Er-lasers [43]. Efficient and power scalable 2.8-μm lasers employing both single-crystals and ceramic Er^{3+}-doped sesquioxide gain media have been reported [39-41].

In the present work, we aimed to perform a systematic spectroscopic study of Er^{3+} ions in solid-solution yttria-scandia, $(Sc_xY_{1-x})_2O_3$, transparent ceramics, focusing on the effect of the Sc^{3+} content on inhomogeneous spectral line broadening and site distribution for the dopant ions, as well as to demonstrate low-threshold laser operation of such "mixed" ceramic gain media at 2.8 μm. Er^{3+}-doped solid-solution ceramic gain media are envisioned as promising laser materials for mode-locked lasers around 2.8 μm.

Note that A_2O_3 compounds exhibit two non-equivalent rare-earth sites with symmetries C_2 (about 3/4 of species) and C_{3i} (1/4 of species). The difficulty in quantifying the spectroscopic properties and the distribution of dopant ions residing in C_{3i} sites lies in the fact that they are "silent" as the electric-dipole transitions are forbidden due to the presence of a center of inversion [44]. Because of this, the C_{3i} RE^{3+} species in cubic sesquioxides remain in the shadows. Here, we propose an original method of their quantification based on the transition probabilities of Er^{3+} ions.

2. Materials and methods

2.1 Fabrication of ceramics

In the present work, transparent ceramics based on Er^{3+}-doped yttria-scandia $(Sc_xY_{1-x})_2O_3$ solid-solutions were fabricated by solid-state vacuum sintering of nanopowders having a complex chemical composition synthesized by the laser ablation method [45]. In brief, the radiation from an ytterbium fiber laser (LS-1, IPG Photonics) was used for ablation of a solid target material made by uniaxial pressing and sintering of commercial oxide powders dry-mixed in the proportion of $Er_{0.14}(Sc_xY_{1-x})_{1.86}O_3$, where $x = 0$, 0.125, 0.25, and 0.5. The vapor phase formed under the laser action was cooled by an air flow to condense and crystallize in the form of nano-sized particles, which were then carried and collected into a bag filter. A minor fraction of the larger particles, such as melt droplets and coarse fragments of the target material was extracted from the nanopowder via sedimentation in ethyl alcohol. From Inductively Coupled Plasma Mass Spectrometry (ICP-MS) analysis (Optima 2100 DV, Perkin Elmer), we determined the

chemical composition of the obtained nanoparticles as follows: $(Er_{0.075}Y_{0.925})_2O_3$, $(Er_{0.074}Sc_{0.114}Y_{0.812})_2O_3$, $(Er_{0.073}Sc_{0.227}Y_{0.700})_2O_3$, and $(Er_{0.072}Sc_{0.445}Y_{0.483})_2O_3$, for x = 0, 0.125, 0.25, and 0.5, respectively. The resulted batches of nanopowders after sedimentation were calcined in air at 600 °C for 3 h for removing residual organics and then compacted at a pressure of 200 MPa into cylindrical-shaped green bodies with a diameter of 14 mm. Vacuum sintering of powder compacts was conducted at 1750 °C for 5 h, followed by annealing in air at 1400 °C for 2 h. The thickness of the fabricated ceramic samples was 1.8 mm after grinding and polishing.

The Er^{3+} ion density in the fabricated ceramics N_{Er} was 4.01×10^{21} at/cm^3, 4.04×10^{21} at/cm^3, 4.07×10^{21} at/cm^3, and 4.21×10^{21} at/cm^3, for x = 0, 0.125, 0.25, and 0.5, respectively.

2.2 Characterization methods

The absorption spectra of the ceramics were measured using a Perkin-Elmer LAMBDA 1050 spectrophotometer with a resolution of 0.75 nm.

The mid-infrared luminescence was excited using a Ti:sapphire laser (Coherent, Mira) tuned to 981 nm, collected using a large mode area ZrF_4 fiber and detected with an optical spectrum analyzer (OSA, Yokogawa AQ6376) purged with N_2 gas to eliminate the structured water vapor absorption in the air. The effect of the residual water absorption was further removed by calibrating the OSA spectral response with a 20 W quartz lamp.

The luminescence decay was studied under excitation by a ns optical parametric oscillator (Horizon, Continuum) tuned to 966 nm and 1460 nm, and the decay curves were measured employing a 1/4 m monochromator (Oriel 77200), an InGaAs detector with a preamplifier (DPCHA-100, Femto) and an 8 GHz oscilloscope (DSA70804B, Tektronix).

The low-temperature (LT, 12 K) spectroscopy studies were performed by cooling down the ceramic samples by means of an APD DE-202 closed-cycle cryo-cooler equipped with an APD HC 2 Helium vacuum cryo-compressor and a Lakeshore 330 temperature controller. The LT absorption spectroscopy was performed with a quartz lamp with a calibrated spectrum, collecting the light transmitted through the samples with OSAs (Ando AQ6315A, Yokogawa AQ6370D). For measuring the LT emission spectra, the three above-mentioned OSAs were also employed.

3. Optical spectroscopy

3.1 Optical absorption

There exist three common pump transitions for mid-infrared Erbium lasers related to excitation into the $^4I_{9/2}$, $^4I_{11/2}$, and $^4I_{13/2}$ manifolds. The corresponding absorption spectra for the Er:$(Sc_xY_{1-x})_2O_3$ ceramics are shown in Fig. 1. The spectral peaks broaden and are reduced in intensity with the gradual increase of the Sc content in the ceramics owing to a significant inhomogeneous spectral line broadening induced by the compositional disorder. It is related to the substantial difference in the ionic radii of Er^{3+} (0.89 Å), Y^{3+} (0.9 Å) and Sc^{3+} (0.745 Å) for VI-fold oxygen coordination [46].

In particular, the $^4I_{15/2} \rightarrow {}^4I_{11/2}$ absorption band can be addressed by commercial spatially multimode high-power InGaAs laser diodes [41], as well as high-brightness Yb fiber lasers (YFL) [47] both emitting at ~0.98 μm. For the parent $(Er_{0.075}Y_{0.925})_2O_3$ ceramic, the maximum absorption cross-section σ_{abs} is 2.55×10^{-21} cm^2 at 981.1 nm corresponding to an absorption bandwidth (FWHM) of only 1 nm. For the $(Er_{0.073}Sc_{0.227}Y_{0.700})_2O_3$ "mixed" ceramic, the maximum σ_{abs} is slightly smaller, 2.50×10^{-21} cm^2 at 981.1 nm, while the absorption bandwidth increases to 3.2 nm. At shorter wavelengths, the broadening effect is even more pronounced and another intense structureless peak appears at 970.2 nm ($\sigma_{abs} = 1.58\times10^{-21}$ cm^2) looking more attractive for diode-pumping.

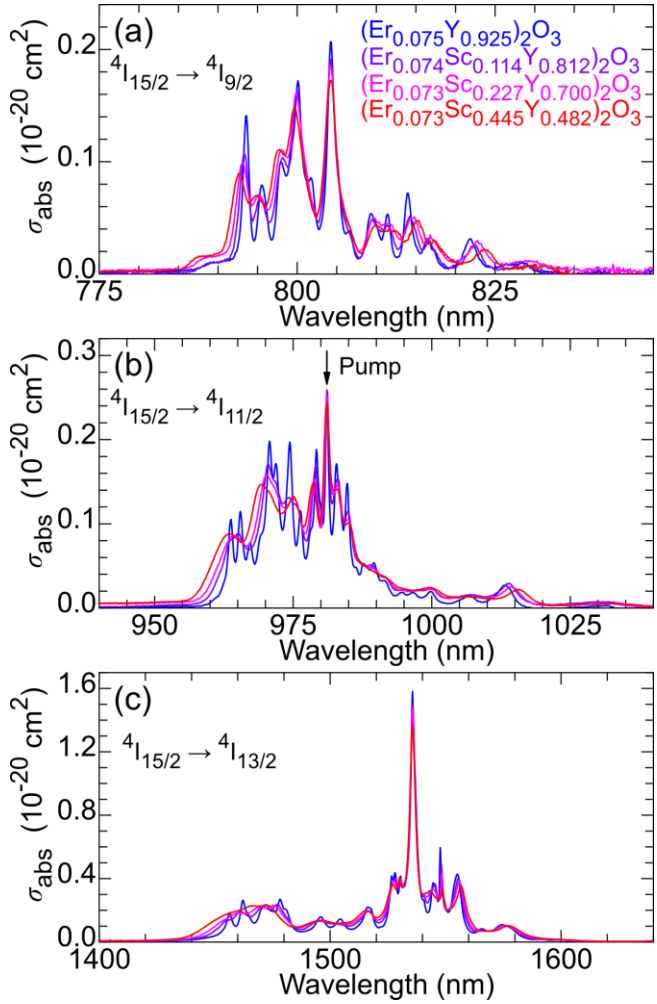

Figure 1. Absorption cross-section, σ_{abs}, spectra of Er^{3+} ions in $(Sc_xY_{1-x})_2O_3$ ceramics for (a) the $^4I_{15/2} \rightarrow {}^4I_{9/2}$ transition, (b) the $^4I_{15/2} \rightarrow {}^4I_{11/2}$ transition, and (c) the $^4I_{15/2} \rightarrow {}^4I_{13/2}$ transition.

The full absorption spectrum of the parent $(Er_{0.075}Y_{0.925})_2O_3$ ceramic was used to determine the absorption and emission transition probabilities of Er^{3+} ions within the parametrization scheme known as the intermediate configuration interaction (ICI) model [48,49]. The

contribution of magnetic dipole (MD) transitions was calculated separately within the Russell-Saunders approximation on Er^{3+} wave functions under a free-ion assumption. The refractive index of Y_2O_3 was calculated from the dispersion formula reported by Zelmon *et al.* [50]. The set of reduced squared matrix elements $U^{(k)}$, $k = 2, 4, 6$, was calculated in this work using the free-ion parameters provided by Yeung and Tanner [51].

In the ICI model, the electric dipole (ED) line strengths $S^{ED}(JJ')$ for $J \rightarrow J'$ transitions are determined as:

$$S_{calc}^{ED}(JJ') = \sum_{k=2,4,6} U^{(k)} \tilde{\Omega}_k, \tag{1a}$$

$$\tilde{\Omega}_k = \Omega_k [1 + 2R_k (E_J + E_{J'} - 2E_f^0)], \tag{1b}$$

where the intensity parameters $\tilde{\Omega}_k$ are linear functions of the energies E_J and $E_{J'}$ of the multiplets involved in the transition $J \rightarrow J'$, E_f^0 is the average energy of the $4f^n$ configuration, and R_k ($k = 2, 4, 6$) are the parameters of interaction with excited configurations. There are six free parameters, Ω_k and R_k for $k = 2$, 4, and 6, each. In the case of $R_k \rightarrow 0$, Equation (1) turns into the formula for the standard J-O model.

Table 1 lists the experimental and calculated (ED + MD) absorption oscillator strengths for Er^{3+} ions. The root-mean-square deviation between them, f_{exp} and f_{calc}, respectively, is relatively low, $\sigma_{RMS} = 0.163$. The best-fit intensity parameters are $\Omega_2 = 4.478$, $\Omega_4 = 1.511$, $\Omega_6 = 0.479$ [10^{-20} cm^2] and $R_2 = -0.048$, $R_4 = 0.092$, $R_6 = 0.002$ [10^{-4} cm].

Table 1. Absorption oscillator strengths[a] of Er^{3+} ions in the parent $(Er_{0.075}Y_{0.925})_2O_3$ ceramic.

$^4I_{15/2} \rightarrow {}^{2S+1}L_J$	E_J, cm^{-1}	Γ, 10^{-20}cm^{2}nm	f_{exp}, 10^{-6}	f_{calc}, 10^{-6} (ICI)
$^4I_{13/2}$	6626	29.052	1.429	0.782^{ED} + 0.608^{MD}
$^4I_{11/2}$	10139	3.680	0.433	0.430^{ED}
$^4I_{9/2}$	12383	1.648	0.288	0.325^{ED}
$^4F_{9/2}$	15198	7.885	2.049	2.012^{ED}
$^4S_{3/2} + {}^2H_{11/2}$	18986	23.223	9.552	9.552^{ED}
$^4F_{7/2}$	20334	2.759	1.298	1.442^{ED}
$^4F_{5/2} + {}^4F_{3/2}$	22121	0.866	0.480	0.512^{ED}
$^2G_{9/2}$	24433	1.174	0.794	0.511^{ED}
$^4G_{11/2} + {}^2K_{15/2} + {}^4G_{9/2} + {}^2G_{7/2}$	26466	27.433	21.714	21.640^{ED} + 0.072^{MD}
σ_{RMS}				*0.163*

[a] E_J – mean transition energy; Γ – integrated absorption cross-section; f_{exp}, f_{calc} – experimental and calculated oscillator strengths, respectively; ED – electric dipole; MD – magnetic dipole; σ_{RMS} – room mean square deviation.

The probabilities of spontaneous radiative transitions A(JJ') (ED + MD), the luminescence branching ratios B(JJ') and the radiative lifetimes of the excited states τ_{rad} are listed in Table 2. For the $^4I_{11/2}$ multiplet, τ_{rad} = 5.39 ms and the luminescence branching ratio for the $^4I_{11/2} \rightarrow {}^4I_{13/2}$ transition B(JJ') is 18.3%.

Table 2. Probabilities[a] of spontaneous radiative transitions of Er^{3+} ions in the parent $(Er_{0.075}Y_{0.925})_2O_3$ ceramic calculated within the ICI model.

$^{2S+1}L_J \rightarrow$	$^{2S'+1}L'_{J'}$	λ_{em}, nm	B(JJ'), %	A(JJ'), s^{-1}	A_{tot}, s^{-1}	τ_{rad}, ms
$^4I_{13/2} \rightarrow$	$^4I_{15/2}$	1509	100	$97.19^{ED} + 75.65^{MD}$	172.84	5.79
$^4I_{11/2} \rightarrow$	$^4I_{13/2}$	2847	18.3	$18.21^{ED} + 15.78^{MD}$	185.34	5.39
	$^4I_{15/2}$	986.3	81.7	151.35^{ED}		
$^4I_{9/2} \rightarrow$	$^4I_{11/2}$	4456	1.4	$1.11^{ED} + 2.41^{MD}$	248.31	4.03
	$^4I_{13/2}$	1737	14.7	36.56^{ED}		
	$^4I_{15/2}$	807.6	83.9	208.23^{ED}		
$^4F_{9/2} \rightarrow$	$^4I_{9/2}$	3552	0.5	$5.71^{ED} + 4.65^{MD}$	2165.7	0.46
	$^4I_{11/2}$	1977	3.4	$61.92^{ED} + 11.44^{MD}$		
	$^4I_{13/2}$	1167	5.2	113.66^{ED}		
	$^4I_{15/2}$	658.0	90.9	1968.3^{ED}		
$^4S_{3/2}+{}^2H_{11/2} \rightarrow$	$^4F_{9/2}$	2640	0.3	$36.66^{ED} + 0.30^{MD}$	14120	0.07
	$^4I_{9/2}$	1515	1.5	$209.54^{ED} + 1.36^{MD}$		
	$^4I_{11/2}$	1130	1.2	$158.19^{ED} + 16.44^{MD}$		
	$^4I_{13/2}$	809.1	5.0	$564.47^{ED} + 135.85^{MD}$		
	$^4I_{15/2}$	526.7	92.0	12998^{ED}		

[a] λ_{em} – mean emission wavelength; B(JJ') – luminescence branching ratio; A(JJ') – probability of spontaneous radiative transition; ED – electric dipole; MD – magnetic dipole; A_{tot} – total radiative transition probability from a $^{2S+1}L_J$ manifold, τ_{rad} – its radiative lifetime.

3.2 Emission (spectra and lifetimes)

The stimulated-emission (SE) cross-sections, σ_{SE}, for the $^4I_{11/2} \rightarrow {}^4I_{13/2}$ transition of Er^{3+} ions in the studied ceramics were calculated using the Füchtbauer-Ladenburg (F-L) equation [52]:

$$\sigma_{SE}(\lambda) = \frac{\lambda^5}{8\pi \langle n \rangle^2 \tau_{rad} c} \frac{B(JJ') W'(\lambda)}{\int \lambda W'(\lambda) d\lambda}, \quad (2)$$

where λ is the light wavelength, $<n>$ is the refractive index at the mean emission wavelength, τ_{rad} is the radiative lifetime of the emitting state (the $^4I_{11/2}$ manifold of Er^{3+}), c is the speed of light, B(JJ') is the luminescence branching ratio, and $W'(\lambda)$ is the measured luminescence spectrum corrected for the effect of the water vapor absorption and the apparatus response of the set-up. The τ_{rad} and B(JJ') values calculated by the ICI theory for Er^{3+} ions in yttria, Y_2O_3, were used. The refractive indices were calculated based on the dispersion curves reported in [50]. For Y_2O_3 at 2.8 μm, n = 1.877.

The σ_{SE} spectra for the Er:$(Sc_xY_{1-x})_2O_3$ (x = 0 – 0.445) ceramics are given in Fig. 2(a). For the parent $(Er_{0.075}Y_{0.925})_2O_3$ ceramic, the maximum SE cross-section is 1.11×10^{-20} cm^2 at 2717 nm

(the zero-phonon line (ZPL) in emission at room temperature) with an emission bandwidth (FWHM) of 5 nm and at longer wavelengths, a weaker ($\sigma_{SE} = 0.62\times10^{-20}$ cm^2) and broader (emission bandwidth: 22 nm) peak appears at 2842 nm. On increasing the Sc^{3+} content in the ceramics, the emission spectra become less structured, and the emission peaks experience a progressive red shift. This is due to the inhomogeneous spectral line broadening induced by the compositional disorder (a partial substitution of Y^{3+} by Sc^{3+}), and an increase of the crystal-field strength for Er:Sc_2O_3 as compared to Er:Y_2O_3. For the "mixed" ceramic with a composition of $(Er_{0.073}Sc_{0.227}Y_{0.700})_2O_3$, the maximum σ_{SE} is reduced to 0.84×10^{-20} cm^2 at 2717 nm (ZPL in emission) and 0.38×10^{-20} cm^2 at 2845 nm (the long-wave emission peak) and the corresponding emission linewidths are broadened to 27 nm (several peaks are merged) and 34 nm, respectively.

The $^4I_{11/2} \rightarrow {}^4I_{13/2}$ transition represents a quasi-three-level laser scheme due to a non-negligible reabsorption from the terminal laser level. Indeed, as the latter constitutes a long-living (metastable) state, the resonant excited-state absorption (ESA) $^4I_{13/2} \rightarrow {}^4I_{11/2}$ has to be taken into account. The ESA cross-sections, σ_{ESA}, of Er^{3+} ions in the $(Sc_xY_{1-x})_2O_3$ ceramics were calculated using the reciprocity method [53]:

$$\sigma_{\mathrm{ESA}} = \sigma_{SE} \cdot \frac{Z_u}{Z_l} \cdot \exp\left(\frac{\frac{hc}{\lambda} - E_{ZPL}}{k_B T}\right), \quad (3)$$

where h is the Planck constant (hc/λ is the photon energy), E_{ZPL} is the ZPL energy (the energy of transition between the lowest-lying crystal-field sub-levels of the two involved multiplets), k_B is the Boltzmann constant, T is the temperature (RT), and $Z_{u(l)}$ are the partition functions for the upper (u) and lower (l) multiplets:

$$Z_{u(l)} = \sum_i g_{i,u(l)} \exp\left(-\frac{E_{i,u(l)}}{k_B T}\right), \quad (4)$$

where E_i is the energy of the i-th sub-level measured from the lower-lying one and g_i is the degeneracy of this sub-level. For calculations, we used the data on the crystal-field splitting for Er^{3+} ions in C_2 symmetry sites in the $(Er_{0.075}Y_{0.925})_2O_3$ ceramic determined in the present work. The ESA cross-section spectra are plotted in Fig. 2(b). For the $(Er_{0.075}Y_{0.925})_2O_3$ ceramic, the maximum σ_{ESA} is 1.16×10^{-20} cm^2 at 2717 nm (the ZPL transition) and 0.22×10^{-20} cm^2 at 2842 nm (the long-wave emission peak).

According to the determined SE and ESA spectra, we calculated the gain cross-sections, $\sigma_{gain} = \beta \cdot \sigma_{SE} - (1 - \beta) \cdot \sigma_{ESA}$, where β is the population inversion ratio, $\beta = N(^4I_{11/2})/(N(^4I_{11/2}) + N(^4I_{13/2}))$ representing the upper-laser-level population relative to the total population of the $^4I_{13/2}$ and $^4I_{11/2}$ manifolds. For the sake of brevity, we only show the gain profiles for the $(Er_{0.074}Sc_{0.227}Y_{0.700})_2O_3$ "mixed" ceramic, see Fig. 2(c). For $\beta < 0.65$, due to the reabsorption induced by ESA from the terminal laser level, the band centered at ~2845 nm dominates in the gain spectra, while for higher inversion ratios, laser emission at the ZPL at 2717 nm is also expected.

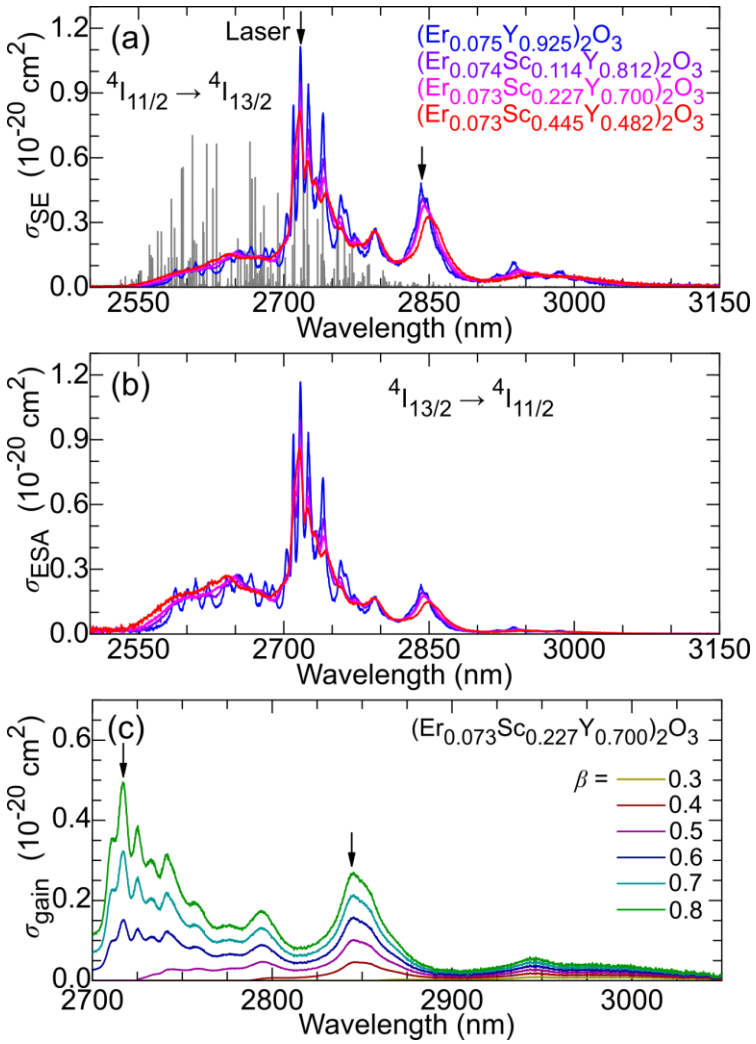

Figure 2. Stimulated emission (SE) and excited-state absorption (ESA) of Er^{3+} ions in $(Sc_xY_{1-x})_2O_3$ ceramics: (a) SE cross-sections, σ_{SE}, for the $^4I_{11/2} \rightarrow {}^4I_{13/2}$ transition; (b) ESA cross-sections, σ_{ESA}, for the $^4I_{13/2} \rightarrow {}^4I_{11/2}$ transition; (c) gain cross-section, σ_{gain}, spectra for the $(Er_{0.074}Sc_{0.227}Y_{0.700})_2O_3$ ceramic for different population inversion ratios β. *Gray lines* – structured water absorption (HITRAN spectroscopic database); *arrows* – observed laser emission lines.

The luminescence decay curves from the upper ($^4I_{11/2}$) and lower ($^4I_{13/2}$) levels for the mid-infrared laser transition of Er^{3+} ions in the Er:$(Sc_xY_{1-x})_2O_3$ ($x = 0 – 0.445$) ceramics are plotted in Fig. 3(a–d) in the semi-log scale. The decay was studied under resonant excitation to the emitting state ($^4I_{11/2}$: $\lambda_{exc} = 966$ nm, $\lambda_{lum} = 1020$ nm and $^4I_{13/2}$: $\lambda_{exc} = 1460$ nm, $\lambda_{lum} = 1560$ nm). The ceramic samples were finely powdered to avoid the detrimental effect of radiation trapping (reabsorption) on the measured lifetimes. The decay from both the $^4I_{13/2}$ and $^4I_{11/2}$ manifolds clearly deviates from the single-exponential law which is ascribed to strong energy-transfer upconversion (ETU) processes from these levels, $^4I_{13/2} + {}^4I_{13/2} \rightarrow {}^4I_{15/2} + {}^4I_{9/2}$ (ETU_1) and $^4I_{11/2} + {}^4I_{11/2} \rightarrow {}^4I_{15/2} + {}^4F_{7/2}$ (ETU_2), with the first process being more efficient. The ETU_1

process favors laser emission at 2.8 μm as it recycles the populations in favor of the upper laser level ($^4I_{11/2}$).

For the parent $(Er_{0.075}Y_{0.925})_2O_3$ ceramic, the mean luminescence lifetimes $<\tau_{lum}>$ of the $^4I_{11/2}$ and $^4I_{13/2}$ states amount to 1.42 ms and 1.26 ms, respectively. The $^4I_{11/2}$ Er^{3+} manifold is subject to multiphonon non-radiative relaxation especially for oxide host materials due to the relatively small energy-gap to the lower-lying state, ΔE, of about 3300 cm^{-1}. Indeed, the "energy-gap" law states that the non-radiative relaxation becomes nearly negligible if the condition $\Delta E/h\nu_{ph,max} >> 5$ is satisfied. For the parent ceramic, the maximum phonon energy $h\nu_{ph,max}$ is 592 cm^{-1} (being relatively low for oxide matrices), so the "energy-gap" law indicates a non-negligible non-radiative path. By adding Sc^{3+} to the ceramic composition, the phonon spectrum is shifted to higher energies, so that shorter luminescence lifetimes of the $^4I_{11/2}$ level are expected. Indeed, $<\tau_{lum}>$ is reduced from 1.42 ms (no Sc^{3+}) to 0.84 ms (44.5 at.% Sc^{3+}).

Both the positive effect of the Sc^{3+} addition on the inhomogeneous spectral broadening and its negative effect on the upper laser level ($^4I_{11/2}$) lifetime shortening should be considered when selecting the optimum ceramic composition. An additional selection criterion is the presence of pores in the "mixed" ceramics deteriorating their optical quality, as well as the drop in the thermal conductivity of ceramics upon Sc^{3+} addition. Based on these considerations, we have selected the $(Er_{0.074}Sc_{0.227}Y_{0.700})_2O_3$ "mixed" ceramic for laser experiments. For this ceramic, $<\tau_{lum}>$ of the $^4I_{11/2}$ and $^4I_{13/2}$ states is 1.37 ms and 1.73 ms, respectively.

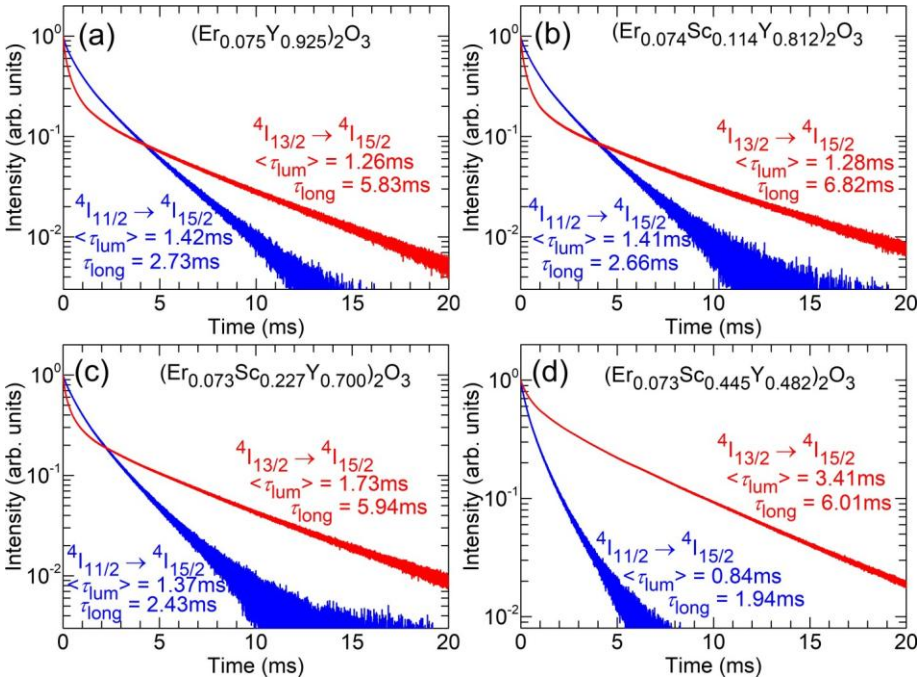

Figure 3. Luminescence decay curves from the $^4I_{11/2}$ and $^4I_{13/2}$ manifolds of Er^{3+} ions in $(Sc_xY_{1-x})_2O_3$ ceramics measured under resonant excitation, $<\tau_{lum}>$ – mean luminescence lifetime, τ_{long} – lifetime achieved by fitting the exponential tail of the decay curve.

3.3 Low-temperature spectroscopy

Er^{3+} ions in cubic sesquioxides A_2O_3 reside in two non-equivalent crystallographic sites with the symmetries C_2 (Wyckoff: 24*d*) and C_{3i} (Wyckoff: 8*b*). In an ideal undistorted sesquioxide lattice, the A^{3+} cations are distributed over these sites in the proportions of 3/4 and 1/4, respectively. For both sites, the A^{3+} cations are VI-fold coordinated by oxygen. For dopant ions residing in C_{3i} symmetry sites, the electric dipole (ED) transitions are strictly forbidden due to the presence of a center of inversion (*i*) and only magnetic dipole (MD) transitions following the selection rules $\Delta J = 0, \pm 1$ are allowed. Thus, ions occupying C_{3i} sites will reveal themselves only for a small number of optical transitions with a MD component and will be silent for purely ED transitions. For ions residing in C_2 sites, both ED and MD are allowed.

In the present work, the LT spectroscopy was used as a tool to i) observe the experimental crystal-field splitting of three Er^{3+} multiplets relevant for mid-infrared laser emission, namely $^4I_{11/2}$ (upper laser level), $^4I_{13/2}$ (lower laser level) and $^4I_{15/2}$ (ground-state), ii) to reveal the effect of Sc^{3+} addition on the inhomogeneous spectral broadening in "mixed" ceramics and iii) to evidence the presence of Er^{3+} ions in C_{3i} sites and to quantify their relative fraction.

Both LT absorption and emission spectra were measured to access the crystal-field splitting of the excited and ground states. In the C_2 symmetry crystal field, each $^{2S+1}L_J$ multiplet with a half-integer J will be split into a total of J + 1/2 Stark sub-levels, *i.e.*, 6, 7 and 8 for $^4I_{11/2}$, $^4I_{13/2}$, and $^4I_{15/2}$, respectively. Following Gruber *et al.* [54], these sub-levels are labelled as A_m, Y_k and Z_i (*m*, *k*, *i* = 1, 2, .. J + 1/2 in increasing energy order). For the assignment of electronic transitions, it was assumed that at 10 K, only the lowest-lying Stark sub-level is populated.

Two transitions in absorption were considered, $^4I_{15/2} \rightarrow {}^4I_{11/2}$ ($Z_1 \rightarrow A_k$, ED, at ~1 μm) and $^4I_{15/2} \rightarrow {}^4I_{13/2}$ ($Z_1 \rightarrow Y_m$, ED + MD, at ~1.5 μm), Fig. 4. The LT absorption spectra were plotted versus the photon energy expressed in cm^{-1} giving access to the splitting of the $^4I_{11/2}$ and $^4I_{13/2}$ excited-states, respectively.

Three transitions in emission were observed, $^4I_{11/2} \rightarrow {}^4I_{15/2}$ ($A_1 \rightarrow Z_i$, ED, at ~1 μm), $^4I_{13/2} \rightarrow {}^4I_{15/2}$ ($Y_1 \rightarrow Z_i$, ED + MD, at ~1.5 μm), $^4I_{11/2} \rightarrow {}^4I_{13/2}$ ($A_1 \rightarrow Y_m$, ED + MD, at ~2.8 μm), as depicted in Fig. 5. This set of optical transition was selected for the following reasons: i) to access the Stark splitting of the ground-state, and ii) by observing at least two transitions terminating at the same multiplet (with one of them of purely ED nature and one – of ED + MD nature), to separate the lines related to Er^{3+} ions residing in C_2 and C_{3i} sites. The LT emission spectra were plotted vs. E_{ZPL} – photon energy (in cm^{-1}), where E_{ZPL} is the ZPL energy of transition for ions in C_2 sites.

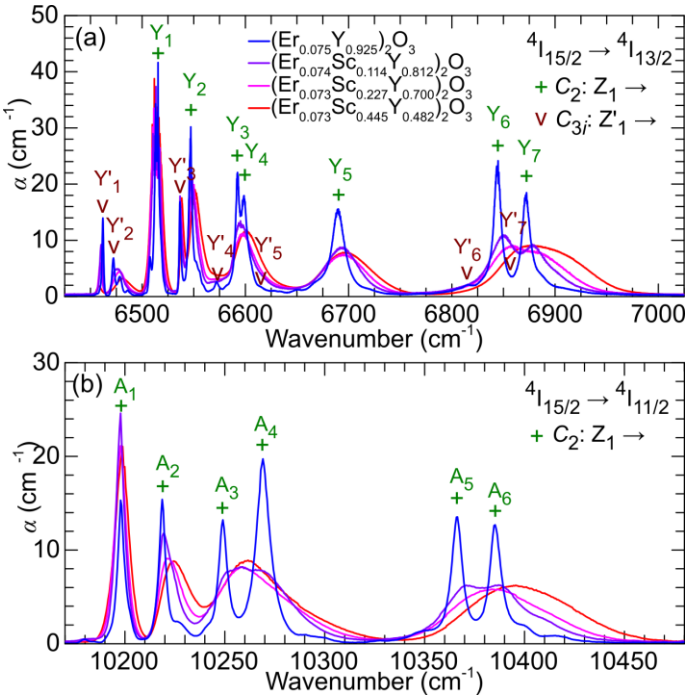

Figure 4. LT (12 K) absorption spectra of Er^{3+} ions in the $(Sc_xY_{1-x})_2O_3$ ceramics: (a) the $^4I_{15/2} \rightarrow {}^4I_{13/2}$ transition (ED + MD) and (b) the $^4I_{15/2} \rightarrow {}^4I_{11/2}$ transition (ED). + and ∨ mark the electronic transitions of Er^{3+} ions in the C_2 and C_{3i} sites, respectively.

Crystal-field splitting. First, we consider the parent ceramic $(Er_{0.075}Y_{0.925})_2O_3$. Even though it does not present inhomogeneous spectral line broadening due to the Sc^{3+} admixture, the LT spectra can be broadened due to the effect of heavy Er^{3+} doping and the ceramic nature of the host matrix. The LT absorption and emission spectra of this ceramic reveal a number of well-resolved intense lines related to electronic transitions of Er^{3+} ions. By excluding the lines assigned to C_{3i} sites (see below), one arrives at the full set of Stark components for the $^4I_{11/2}$, $^4I_{13/2}$, and $^4I_{15/2}$ multiplets of C_2 species, see Table 3. For the 2.8-μm transition of Er^{3+} ions, the calculated partition functions at RT amount to Z_u ($^4I_{11/2}$) = 0.704 and Z_l ($^4I_{13/2}$) = 0.569, so that $Z_u/Z_l = 1.238$ and the ZPL energy E_{ZPL} is 3684 cm^{-1}. The total Stark splitting of the $^4I_{13/2}$ and $^4I_{15/2}$ states is relatively large, namely 358 cm^{-1} and 504 cm^{-1}, respectively, owing to the high crystal-field strength inherent to cubic sesquioxides.

Inhomogeneous spectral broadening. The LT absorption and emission spectra of "mixed" ceramics show a similar behavior upon increasing the Sc^{3+} content in the ceramics: i) the spectra progressively broaden, and individual electronic transitions become non-resolved and ii) a notable shift to higher wavenumbers occurs. It is remarkable that the first effect is clear even for a relatively small Sc^{3+} content of 11.4 at.%. The first effect is related to the compositional disorder promoted by the large difference in ionic radii of Y^{3+} and Sc^{3+}. The spectral shifts are due to the increased crystal-field strength for Sc_2O_3 as compared to Y_2O_3. Assessing the spectral linewidths (FWHM) of LT absorption peaks allowed us to trace the energy diagram of crystal-

field split $^4I_{11/2}$ and $^4I_{13/2}$ manifolds of Er^{3+} ions residing in C_2 sites in $(Sc_xY_{1-x})_2O_3$ ceramics. Figure 6 illustrates the dependence of the sub-level positions and widths as a function of Sc^{3+} content: it is noticeable that even at low Sc^{3+} concentrations, some of the sublevels broaden enough to overlap, while the overall barycenter of the multiplet gradually shifts to higher energies and so does the total Stark splitting. For example, for transitions from the lower-lying Stark sub-level of the ground-state $^4I_{15/2}$ (Z_1) to the pair of higher lying sub-levels of the $^4I_{13/2}$ excited manifold (Y_6 and Y_7), the peak linewidths $\Delta\nu_0$ are relatively narrow at 12 K, 9.5 cm^{-1} and 10.7 cm^{-1}, respectively, for the parent $(Er_{0.075}Y_{0.925})_2O_3$ ceramic. Even for 11.4 at.% Sc^{3+}, these two separate electronic transitions become undistinguishable and the combined linewidth $\Delta\nu$ progressively increases with the Sc^{3+} content, from 60.7 cm^{-1} for $(Er_{0.074}Sc_{0.114}Y_{0.812})_2O_3$, to 77.1 cm^{-1} for $(Er_{0.074}Sc_{0.227}Y_{0.700})_2O_3$, and further to 89.7 cm^{-1} for $(Er_{0.073}Sc_{0.445}Y_{0.482})_2O_3$, thus representing an enhancement factor for inhomogeneous spectral line broadening ($\Delta\nu/\Delta\nu_0$) of about 9 in the energy scale.

C_{3i} sites. Among the considered transitions in absorption and emission, three were of both ED and MD origin. Below we list these transitions together with the corresponding probabilities calculated by the ICI theory, cf. Table 2: $^4I_{15/2} \leftrightarrow {}^4I_{13/2}$ (both absorption and emission, $A(JJ') = 97.19^{ED} + 75.65^{MD}$ s^{-1}), and $^4I_{11/2} \rightarrow {}^4I_{13/2}$ (emission, $A(JJ') = 18.21^{ED} + 15.78^{MD}$ s^{-1}). The relative contribution of MD probability to the total (ED + MD) one is relatively big in all cases, about 45%. Thus, one can expect a non-negligible contribution of C_{3i} Er^{3+} species to the measured absorption and luminescence spectra even despite the lower fraction of dopant ions residing in these sites (see below).

The extra lines assigned to C_{3i} sites could be unambiguously deduced only for the parent ceramic, as in the presence of a strong inhomogeneous spectral line broadening (for "mixed" ceramics), they are hidden within the broad envelopes combining several electronic lines. For LT absorption spectra, the *x*-axis scale is identical for both C_2 and C_{3i} sites. For LT emission spectra, two different *x*-axis scales are presented (one for C_2 sites, and another one for C_{3i} sites), as ZPLs for both sites are not necessarily the same.

The first attempt to assign the C_{3i} crystal-field energy levels of Er^{3+} ions in yttria was performed in 1972 by Bloor and Dean [55] and it evidences significant challenges. In 1985, Gruber *et al.* performed an extended analysis for two multiplets, $^4I_{15/2}$ and $^4I_{11/2}$, supported by crystal-field calculations [54] and it was refined in 2008 by the same group [44]. In our assignment of the LT absorption spectra, see Fig. 4(a), and emission spectra, cf. Fig. 5(b,c), we followed the interpretation from the latest work by Gruber *et al.* [44] which well matched our spectral data considering small energy shifts in the energy-level position between crystals and ceramics.

All the deduced experimental crystal-field sub-levels of the $^4I_{15/2}$, $^4I_{13/2}$, and $^4I_{11/2}$ multiplets of Er^{3+} ions in C_2 sites in the parent $(Er_{0.075}Y_{0.925})_2O_3$ ceramic are reported in Table 3.

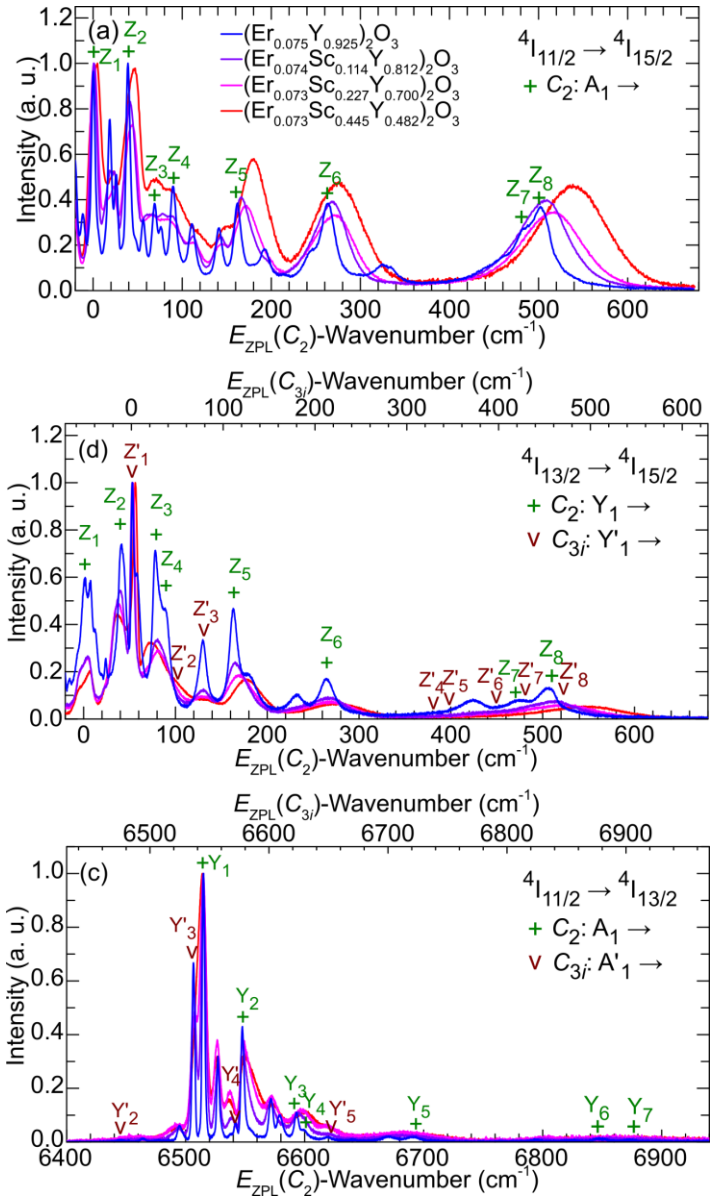

Figure 5. LT (12 K) luminescence spectra of Er^{3+} ions in the $(Sc_xY_{1-x})_2O_3$ ceramics: (a) the $^4I_{11/2} \rightarrow {}^4I_{15/2}$ transition (ED), (b) the $^4I_{13/2} \rightarrow {}^4I_{15/2}$ transition (ED + MD) and (c) the $^4I_{11/2} \rightarrow {}^4I_{13/2}$ transition (ED + MD). + and ∨ mark the electronic transitions of Er^{3+} ions in the C_2 and C_{3i} sites, respectively.

Table 3. Crystal-field splitting of selected Er^{3+} multiplets in $(Er_{0.075}Y_{0.925})_2O_3$.

$Er^{3+}\ {}^{2S+1}L_J$	Sub-level energy (cm^{-1})
$^4I_{15/2}$	0, 39, 78, 90, 163, 264, 482, 504 (C_2)
	0, 47, 78, 322, 329, 399, 439, 484 (C_{3i})
$^4I_{13/2}$	6514, 6547, 6592, 6599, 6690, 6845, 6872 (C_2)
	6462, 6472, 6536, 6572, 6673, 6816, 6853 (C_{3i})
$^4I_{11/2}$	10198, 10219, 10249, 10269, 10366, 10385 (C_2)
	10168 (C_{3i}), *5 missing*

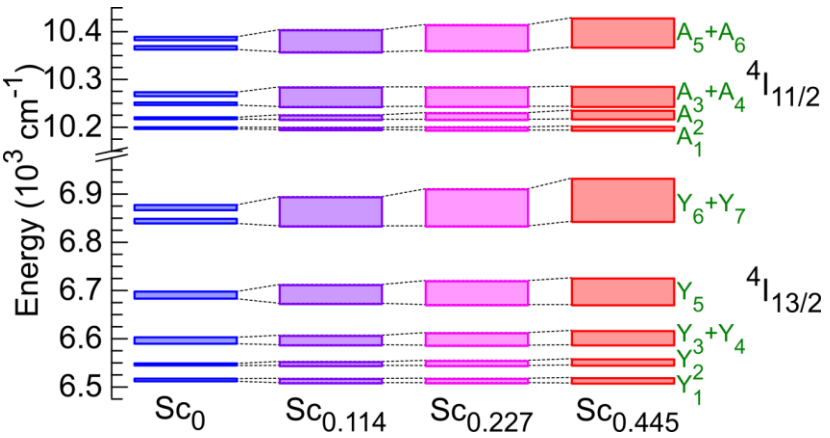

Figure 6. Experimental crystal-field splitting of the $^4I_{13/2}$ and $^4I_{11/2}$ multiplets of Er^{3+} ions in C_2 sites in $(Sc_xY_{1-x})_2O_3$ ceramics obtained from LT (12 K) absorption spectroscopy, indicating both the energy-level position and inhomogeneous spectral linewidths (FWHM) for each resolved Stark sub-level. *Dashed lines* are drawn as guides for the eye.

Fraction of ions in C_{3i} sites. One of the intriguing questions about sesquioxides is the preservation of the ideal 3/4 to 1/4 rare-earth ion distribution over C_2 and C_{3i}, respectively, when the host composition is changed either via doping or solid-solution formation. There exist studies on the evaluation of the rare-earth ion distribution over these sites for parent yttria compounds. Blanusa *et al.* derived a nearly random cationic distribution for Tm^{3+} ions in Y_2O_3 using the Rietveld structure refinement [56] and a similar conclusion was reached by Mitric *et al.* for Yb^{3+} ions [57]. In the present work, we combined the LT absorption spectroscopy and the theory of transition intensities to address this question.

The $^4I_{15/2} \rightarrow {}^4I_{13/2}$ transition in absorption ($Z_1 \rightarrow Y_m$, m = 1 – 7, ED + MD) was selected for the analysis. The parent $(Er_{0.075}Y_{0.925})_2O_3$ ceramic was first considered. A deconvolution of the LT absorption spectrum via a series of Gaussian peaks was performed, allowing us to estimate the position, the spectral linewidth and the area of every peak related to a single electronic transition for both C_2 and C_{3i} sites individually, as depicted in Fig. 7(a). Here, the sub-levels of Er^{3+} ions in C_{3i} sites are labelled with a prime, Y'_m. Figure 7(b) shows the corresponding energy-level diagram of the $^4I_{13/2}$ multiplet. Note the differences in both the position of the ZPL and the total Stark splitting of this multiplet for the two considered sites. The total areas S of all $Z_1 \rightarrow Y_m$ (C_2) and $Z_1 \rightarrow Y'_m$ (C_{3i}) transitions are proportional to the total transition probabilities, $f(JJ')_{C2} = 0.782^{ED} + 0.608^{MD}$ [10^{-6}] and $f(JJ')_{C3i} = 0.608^{MD}$ [10^{-6}], respectively, multiplied by the corresponding site occupancies X_{C2} and X_{C3i}, respectively ($X_{C2} + X_{C3i} = 1$), so that $S_{C2} \sim f(JJ')_{C2} \times X_{C2}$ and $S_{C3i} \sim f(JJ')_{C3i} \times X_{C3i}$. This enabled us to calculate the X_{C2} and X_{C3i} values, according to the following equations:

$$X_{C2}/X_{C3i} = (S_{C2}/S_{C3i}) \times (f(JJ')_{C3i}/f(JJ')_{C2}), \quad (5a)$$

$$X_{C2} + X_{C3i} = 1. \quad (5b)$$

For the parent ceramic, one arrives to S_{C2}/S_{C3i} = 7.08 and X_{C3i} of 0.243, i.e., being very close to the ideal ratio of 1/4. This confirms that doping with Er^{3+} ions, even despite the relatively high substitution level of 7.5 at.%, does not move the 3/4 (C_2) and 1/4 (C_{3i}) distribution. This can be mainly explained by the closeness of ionic radii of Er^{3+} and Y^{3+}.

To accurately estimate the dependence of X_{C3i} on the content of scandium in "mixed" ceramics, it was necessary to study a pair of well-resolved LT absorption peaks associated with C_2 and C_{3i} sites and to determine the ratio of their integral areas ($S_{peak,C2}/S_{peak,C3i}$) for all the studied samples. The $Z_1 \rightarrow Y_2$ (C_2) and $Z'_1 \rightarrow Y'_3$ (C_{3i}) pair of peaks was chosen, as they are relatively close to each other and well resolved even for high Sc^{3+} contents, as depicted in Fig. 7(c). By normalizing the $S_{peak,C2}/S_{peak,C3i}$ ratios to the total S_{C2}/S_{C3i} integral for the parent ceramic, the S_{C2}/S_{C3i} ratio was determined as a function of Sc^{3+} concentration. Finally, the X_{C3i} values were deduced for each ceramic, and are shown in Fig. 7(d). Here, one can see the clear increase in the C_{3i} site fraction as a function of scandium content, a change which is ascribed to the difference in ionic radius between Sc^{3+} and Y^{3+}, and therefore the larger mismatch with the ionic radius of the dopant Er^{3+} ions.

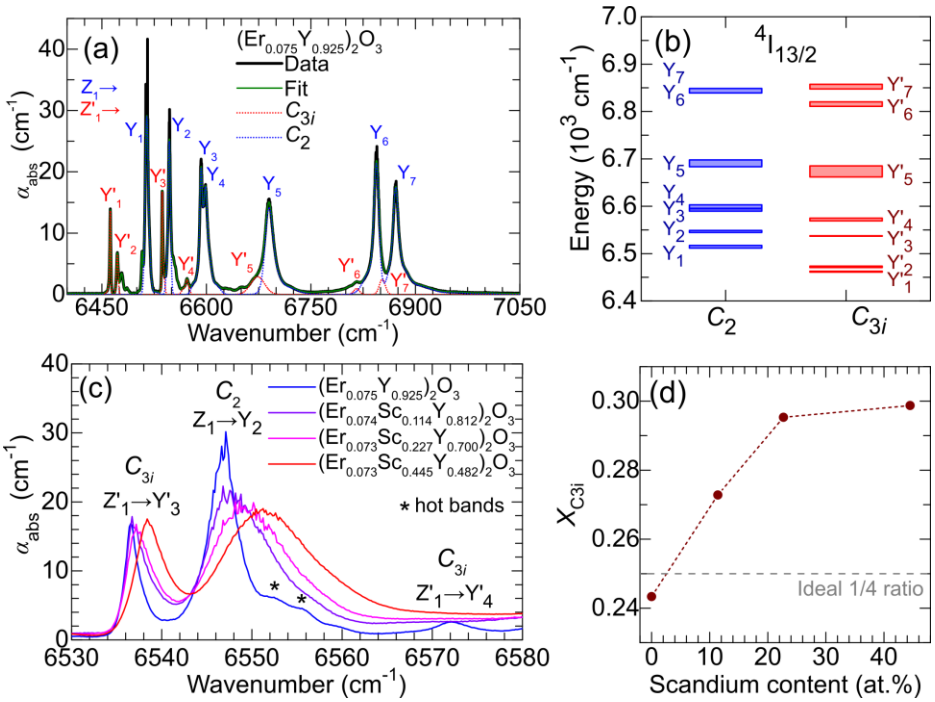

Figure 7. Distribution of Er^{3+} ions over C_2 and C_{3i} symmetry sites in Er:$(Sc_xY_{1-x})_2O_3$ ceramics: (a,b) parent $(Er_{0.075}Y_{0.925})_2O_3$ ceramic: (a) deconvolution of the LT (12 K) absorption spectrum using a series of Gaussian peaks, the $^4I_{15/2} \rightarrow {}^4I_{13/2}$ transition; (b) experimental crystal-field splitting of the $^4I_{13/2}$ multiplet for with C_2 and C_{3i} sites accounting for the inhomogeneous spectral linewidths estimated from the fit; (c) a close look at the $Z_1 \rightarrow Y_2$ (C_2) and $Z'_1 \rightarrow Y'_3$ (C_{3i}) electronic transitions for all studied ceramic compositions, the *asterisks* mark hot peaks assigned to the Z_2 level absorption; (d) the site occupancy X_{C3i} for C_{3i} sites as a function of scandium content.

4. Mid-infrared laser operation

4.1 Laser setup

The laser experiments were carried out with the $(Er_{0.073}Sc_{0.227}Y_{0.700})_2O_3$ "mixed" ceramic sample. The uncoated ceramic element (Φ12 mm, thickness: 1.8 mm) was mounted on a passively cooled Cu holder using a thermal conductive silver paint. The hemispherical cavity was formed by a plane pump mirror (PM) coated for high transmission (HT) at 0.92 – 1.06 μm and high reflection (HR) at 2.6 – 3.0 μm, and a set of concave output couplers (OCs) having a radius of curvature (RoC) of −100 mm and a transmission at the laser wavelength T_{OC} in the range of 0.33% – 4.0%. The ceramic was placed near the PM with a small air gap of less than 1 mm. The total cavity length was ~99 mm. The pump source was a Ti:Sapphire laser (3900S, Spectra Physics) delivering up to 3.5 W at 981.1 nm thus addressing the $^4I_{15/2} \rightarrow {}^4I_{11/2}$ Er^{3+} transition. The near diffraction limited ($M^2 \approx 1$) pump beam was focused into the ceramic element through the PM by an antireflection coated achromatic lens (focal length: $f = 75$ mm). The measured single-pass pump absorption under lasing conditions was weakly dependent on the output coupling and amounted to 53.2%. The residual pump was filtered out using a long-pass filter (LP1400, Spectrogon). The laser spectra were measured using an optical spectrum analyzer (Yokogawa AQ6376) and a ZrF_4 fiber. The setup is depicted in Fig. 8.

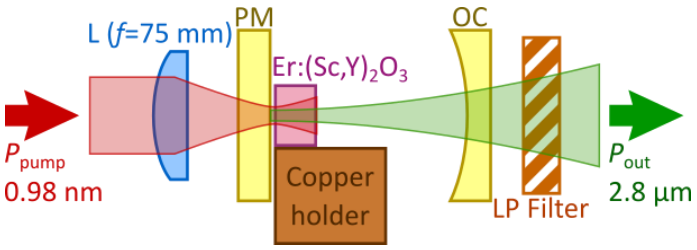

Figure 8. Schematic of the laser setup: L – aspherical focusing lens; PM – flat pump mirror; OC – curved output coupler.

4.2 Mid-infrared ceramic laser

In the continuous-wave operation regime, the ceramic laser generated a maximum output power of 312 mW at 2716 nm with a slope efficiency η of 18.6% (versus the absorbed pump power, fitting the input-output dependence well above the laser threshold of 128 mW) when using an intermediate output coupling of 1.7%, Fig. 9(a). This corresponded to a maximum incident pump power of 3.48 W. No thermal roll-over was observed for the studied range of pump powers. The laser threshold gradually increased with the output-coupling, from 37 mW (T_{OC} = 0.33%) up to 237 mW (T_{OC} = 4.0%). The laser operated on the fundamental transverse mode ($M^2 < 1.2$).

The laser output was unpolarized. The spectra of laser emission measured well above the laser threshold are shown in Fig. 9(b). For T_{OC} = 0.77 – 4.0%, the laser operated at 2714 – 2718 nm in agreement with the maximum of the $^4I_{11/2} \rightarrow {}^4I_{13/2}$ emission band, cf. Fig. 2(a), while for a small T_{OC} = 0.33%, longer laser wavelengths of 2841 – 2853 nm were observed. This behavior is due

to the reabsorption at the laser wavelength induced by the excited-state absorption from the long-living terminal laser level, $^4I_{13/2} \rightarrow {}^4I_{11/2}$, Fig. 2(b). For inversion ratios $\beta < 0.65$, the long-wave peak at 2.85 μm dominates in the gain spectra as shown in Fig. 2(c).

The passive losses in the ceramic element were estimated using the Findlay-Clay analysis, *i.e.*, by plotting the laser threshold P_{th} as a function of $\ln(1/R_{OC})$, where $R_{OC} = 1 - T_{OC}$ is the output coupler reflectivity, Fig. 9(b). The best-fit of experimental points yielded a round-trip passive loss L of 0.88% corresponding to a loss coefficient $\delta = 0.022$ cm^{-1} at ~2.8 μm. This value gives an estimation for scattering losses in the ceramic related to its residual porosity.

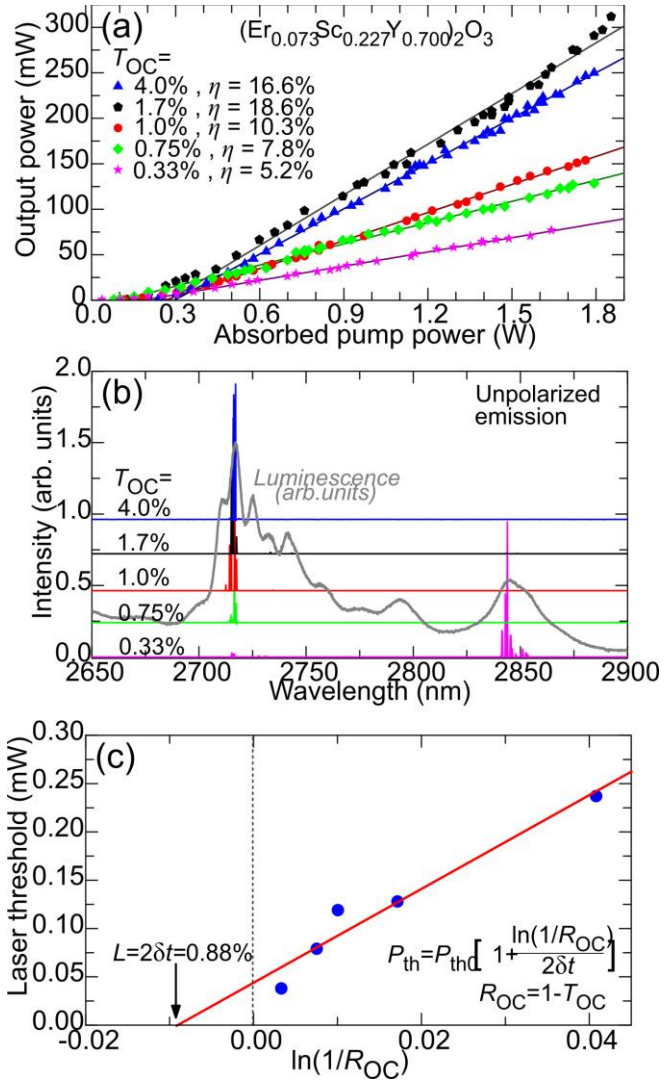

Figure 9. Laser performance of the $(Er_{0.073}Sc_{0.227}Y_{0.700})_2O_3$ ceramic: (a) input-output dependences, η – slope efficiency; (b) typical spectra of laser emission, unpolarized radiation; (c) Findlay-Clay analysis for the determination of the round-trip passive loss L.

5. Conclusions

To conclude, Erbium-doped "mixed" sesquioxide ceramics in the binary system of yttria-scandia are promising gain materials with broadband mid-infrared emission properties around 2.8 μm. The addition of Sc to the ceramics has a complex effect on their microstructure, thermal and vibronic properties of the host matrix (as evidenced in the previous work), as well as the spectroscopic behavior of the dopant Er^{3+} ions (the results obtained here):

i) Effect on the host properties: The Sc addition increases the porosity of ceramics (and, accordingly, losses), degrades their thermal conductivity and increases the maximum phonon energy. Altogether, these changes are unfavorable for laser development;

ii) Effect on the spectroscopic properties: the addition of Sc even as a minority component (i.e., below the $ScYO_3$ composition) provides a strong inhomogeneous spectral line broadening for both the absorption and emission spectra. It is enabled by the compositional disorder (*i.e.*, the difference in the mass and ionic radius of cations composing the second coordination sphere around the Er^{3+} ions). The strong sensitivity of the crystal-field strength in cubic sesquioxides to the nature of the host-forming cation drives this process. As evidenced by low-temperature spectroscopy, an enhancement of the inhomogeneous spectral linewidth by a factor of 9 could be achieved for Er^{3+}-doped yttria-scandia as compared to yttria. The broadening of absorption bands is beneficial for mitigating the sensitivity of Er lasers to the drift of the pump wavelength (*e.g.*, for laser diodes), and broadening and flattening of the gain bandwidth around 2.8 μm is of relevance for continuous wavelength tuning and (potentially) ultrashort pulse generation. However, when approaching the $ScYO_3$ composition, the increased phonon energy of the host matrix plays a negative role in excessive shortening of the luminescence lifetime of the upper laser level manifold, $^4I_{11/2}$, via the increased non-radiative relaxation.

By considering these two concurrent effects, we conclude that Er^{3+}-doped yttria-scandia ceramics with relatively small (about 1/4) Sc contents appear as ideal candidates for laser development, as they combine reasonably good optical quality and thermal properties alongside with the appealing spectroscopic properties. First laser operation of a ceramic with a close composition is demonstrated in the present work.

Our work also proposes an original approach to address a long-lasting question about the distribution of dopant rare-earth ions over C_2 and C_{3i} symmetry sites in cubic sesquioxides, as well as the effect of the "mixed" compositions on this distribution. For the parent ceramic, the distribution is very close to the ideal ratio of 3/4 (C_2) and 1/4 (C_{3i}), even despite the relatively high substitution level of 7.5 at.% Er^{3+}. However, we observe a clear increase in the C_{3i} site population on increasing the scandium content, a change which is ascribed to the difference in the ionic radius between Sc^{3+} and Y^{3+}. This ion redistribution is seen as an additional negative factor, as C_{3i} species almost do not contribute to optical transitions.

Acknowledgements. RFBR (Russia) according to the research project No. 21-53-15014 and CNRS (France) according to the project IEA No. 00432. State task of IEP UrB RAS No. 124022200004-5 (2024-2026). R. M. acknowledges the partial research funding from

the Ministry of Science and Higher Education of the Russian Federation (Ural Federal University Program of Development within the Priority-2030 Program).

Declaration of competing interest

The authors declare that they have no known competing financial interests or personal relationships that could have appeared to influence the work reported in this paper.

Data availability

Data will be made available on request.

References

1. Z. Xiao, S. Yu, Y. Li, Materials development and potential applications of transparent ceramics: a review, Mat. Sci. Eng. R., 139 (2020) 100518.
2. O. J. Akinribide, G. N. Mekgwe, S. O. Akinwamide, F. Gamaoun, C. Abeykoon, O. T. Johnson, P. A. Olubambi, A review on optical properties and application of transparent ceramics, J. Mater. Res. Technol. 21 (2022) 712–738.
3. J. Sanghera, W. Kim, G. Villalobos, B. Shaw, C. Baker, J. Frantz, B. Sadowski, I. Aggarwal, Ceramic laser materials, Materials 5 (2012) 258–277.
4. V. Lupei, A. Lupei, A. Ikesue, Transparent polycrystalline ceramic laser materials, Opt. Mater. 30 (2008) 1781-1786.
5. A. Goldstein, A. Krell, Transparent ceramics at 50: progress made and further prospects, J. Am. Ceram. Soc. 99 (2016) 3173-3197.
6. L. Zhang, Y. Ben, H. Chen, D. Tang, X. Fu, R. Sun, B. Song, C. Wong, Low temperature-sintering and microstructure of highly transparent yttria ceramics, J. Alloys Compd. 695 (2017) 2580–2586.
7. D. Yin, J. Ma, P. Liu, B. Yao, J. Wang, Z. Dong, L. B. Kong, D. Tang, Submicron-grained Yb:Lu_2O_3 transparent ceramics with lasing quality, J. Am. Ceram. Soc. 102 (2019) 2587–2592.
8. T. Epicier, G. Boulon, W. Zhao, M. Guzik, B. Jiang, A. Ikesue, L. Esposito Spatial distribution of the Yb^{3+} rare earth ions in $Y_3Al_5O_{12}$ and Y_2O_3 optical ceramics as analyzed by TEM, J. Mater. Chem. 22 (2012) 18221–18229.
9. K. Eremeev, P. Loiko, A. Braud, P. Camy, J. Zhang, X. Xu, Y. Zhao, P. Liu, S. Balabanov, E. Dunina, A. Kornienko, Spectroscopy of solid-solution transparent sesquioxide laser ceramic Tm: $LuYO_3$, Optical Materials Express 12 (2022) 3749-3762.
10. L. Basyrova, P. Loiko, W. Jing, Y. Wang, H. Huang, E. Dunina, A. Kornienko, L. Fomicheva, B. Viana, U. Griebner, V. Petrov, Spectroscopy and efficient laser operation around 2.8 μm of Er:(Lu, $Sc)_2O_3$ sesquioxide ceramics, Journal of Luminescence 240 (2021) 118373.
11. A. Pirri, R. N. Maksimov, J. Li, M. vannini, G. Toci, Achievements and future perspectives of the trivalent thulium-ion-doped mixed-sesquioxide ceramics for laser applications, Materials 15 (2022) 2084.
12. A. Ikesue, Y. L. Aung, T. Kamimura, S. Honda, Y. Iwamoto, Composite laser ceramics by advanced bonding technology, Materials 11 (2018) 271.

13. F. Tian, A. Ikesue, J. Li, Progress and perspectives on composite laser ceramics: a review, J. Eur. Ceram. Soc. 42 (2022) 1833–1851.
14. W. Liu, J. Li, B. Jiang, D. Zhang, Y. Pan, 2.44 KW laser output of Nd:YAG ceramic slab fabricated by a solid-state reactive sintering, J. Alloys Compd. 538 (2012) 258–261.
15. M. Divoký, J. Pilař, M. Hanuš, P. Navrátil, O. Denk, P. Severová, P. Mason, T. Butcher, S. Banerjee, M. De Vido, C. Edwards, 150 J DPSSL operating at 1.5 kW level, Opt. Lett. 46 (2021) 5771–5773.
16. S. Esser, X. Xu, J. Wang, J. Zhang, T. Graf, M. Abdou Ahmed, Single-crystal and ceramic Yb:Lu_2O_3 gain media for thin-disk oscillators, Appl. Phys. B 129 (2023) 160.
17. L. Mezeix, D. J. Green, Comparison of the mechanical properties of single crystal and polycrystalline yttrium aluminum garnet, Appl. Ceram. Technol. 3 (2006) 166–176.
18. J. Dong, A. Shirakawa, K. I. Ueda, H. Yagi, T. Yanagitani, A. A. Kaminskii, Laser-diode pumped heavy-doped Yb:YAG ceramic lasers, Opt. Lett. 32 (2007) 1890-1892.
19. Y. Feng, G. Toci, B. Patrizi, A. Pirri, Z. Hu, X. Chen, J. Wei, H. Pan, X. Li, X. Zhang, S. Su, Fabrication, microstructure, and optical properties of Tm: $Y_3ScAl_4O_{12}$ laser ceramics, J. Am. Ceram. Soc. 103 (2020) 1819-1830.
20. L. Basyrova, R. Maksimov, V. Shitov, M. Baranov, V. Mikhaylovsky, A. Khubetsov, O. Dymshits, X. Mateos, P. Loiko, Effect of SiO_2 addition on structural and optical properties of Yb:$Lu_3Al_5O_{12}$ transparent ceramics based on laser ablated nanopowders, J. Alloys Compd. 806 (2019) 717-725.
21. Z. Liu, A. Ikesue, J. Li, Research progress and prospects of rare-earth doped sesquioxide laser ceramics, J. Eur. Ceram. Soc. 41 (2021) 3895-3910.
22. W. Jing, P. Loiko, J. M. Serres, Y. Wang, E. Vilejshikova, M. Aguilo, F. Diaz, U. Griebner, H. Huang, V. Petrov, X. Mateos, Synthesis, spectroscopy, and efficient laser operation of "mixed" sesquioxide Tm:$(Lu,Sc)_2O_3$ transparent ceramics, Opt. Mater. Express 7 (2017) 4192-4202.
23. P. Loiko, L. Basyrova, R. Maksimov, V. Shitov, M. Baranov, F. Starecki, X. Mateos, P. Camy, Comparative study of Ho:Y_2O_3 and Ho:$Y_3Al_5O_{12}$ transparent ceramics produced from laser-ablated nanoparticles, J. Lumin. 240 (2021) 118460.
24. M. E. Doroshenko, A. A. Demidenko, P. P. Fedorov, E. A. Garibin, P. E. Gusev, H. Jelinkova, V. A. Konyshkin, M. A., Krutov, S. V. Kuznetsov, V. V. Osiko, P. A. Popov, Progress in fluoride laser ceramics, Phys. Stat. Sol. C 10 (2013) 952-957.
25. Z. Liu, M. Jia, G. Yi, B. Mei, Q. Jing, P. Liu, Fabrication and microstructure characterizations of transparent Er:CaF_2 composite ceramic, J. Am. Ceram. Soc. 102 (2019) 285-293.
26. C. Kränkel, Rare-earth-doped sesquioxides for diode-pumped high-power lasers in the 1-, 2-, and 3-μm spectral range, IEEE J. Sel. Top. Quantum Electron. 21 (2015) 1602013.
27. J. H. Mun, A. Jouini, A. Novoselov, Y. Guyot, A. Yoshikawa, H. Ohta, H. Shibata, Y. Waseda, G. Boulon, T. Fukuda, Growth and characterization of Tm-doped Y_2O_3 single crystals, Opt. Mater. 29 (2007) 1390–1393.
28. W. Jing, P. Loiko, L. Basyrova, Y. Wang, H. Huang, P. Camy, U. Griebner, V. Petrov, J. M. Serres, R. M Solé, M. Aguiló, Spectroscopy and laser operation of highly-doped 10 at.% Yb:$(Lu, Sc)_2O_3$ ceramics, Opt. Mater. 117 (2021) 111128.
29. L. Wang, B. Lu, X. Liu, Y. Shi, J. Li, Y. Liu, Fabrication and upconversion luminescence of novel transparent Er_2O_3 ceramics, J. Eur. Ceram. Soc. 40 (2020) 1767-1772.

30. K. Eremeev, P. Loiko, S. Balabanov, T. Evstropov, D. Permin, O. Postnikova, V. Petrov, P. Camy, A. Braud, Spectroscopy of thulium ions in solid-solution sesquioxide laser ceramics: inhomogeneous spectral line broadening, crystal-field engineering and C_{3i} sites, Opt. Mater. 148 (2024) 114791.
31. M. V. Abrashev, N. D. Todorov, J. Geshev, The equilibrium temperature between solid and liquid phases of yttrium oxide, Rev. Int. Htes. Temp. Refract. 12 (1975) 329–335.
32. K. Petermann, L. Fornasiero, E. Mix, V. Peters, High melting sesquioxides: crystal growth, spectroscopy, and laser experiments, Opt. Mater. 19 (2002) 67–71.
33. V. Peters, A. Bolz, K. Petermann, G. Huber, Growth of high-melting sesquioxides by the heat exchanger method, J. Cryst. Growth 237 (2002) 879–883.
34. R. N. Maksimov, V. A. Shitov, V. V. Platonov, A.S. Yurovskikh, G. Toci, B. Patrizi, M. Vannini, A. Pirri, Hot isostatic pressing of transparent Yb^{3+}-doped Lu_2O_3 ceramics for laser applications," Ceram. Int. 47 (2021) 5168–5176.
35. C. Kränkel, A. Uvarova, É. Haurat, L. Hülshoff, M. Brützam, C. Guguschev, S. Kalusniak, D. Klimm, Czochralski growth of mixed cubic sesquioxide crystals in the ternary system Lu_2O_3–Sc_2O_3–Y_2O_3, Acta Crystallogr. B Struct. Sci. Cryst. Eng. Mater. 77 (2021) 550-558.
36. Y. Zhao, L. Wang, W. Chen, P. Loiko, Y. Wang, Z. Pan, H. Yang, W. Jing, H. Huang, J. Liu, X. Mateos, Kerr-lens mode-locked Tm-doped sesquioxide ceramic laser, Opt. Lett. 46 (2021) 3428-3431.
37. Y. Wang, W. Jing, P. Loiko, Y. Zhao, H. Huang, X. Mateos, S. Suomalainen, A. Härkönen, M. Guina, U. Griebner, V. Petrov, Sub-10 optical-cycle passively mode-locked Tm:$(Lu_{2/3}Sc_{1/3})_2O_3$ ceramic laser at 2 μm, Opt. Express. 26 (2018) 10299-10304.
38. Y. Zhao, L. Wang, Y. Wang, J. Zhang, P. Liu, X. Xu, Y. Liu, D. Shen, J. E. Bae, T. G. Park, F. Rotermund, SWCNT-SA mode-locked Tm: $LuYO_3$ ceramic laser delivering 8-optical-cycle pulses at 2.05 μm, Opt. Lett. 45 (2020) 459-462.
39. T. Li, K. Beil, C. Kränkel, G. Huber, Efficient high-power continuous wave Er:Lu_2O_3 laser at 2.85 μm, Opt. Lett. 37 (2012) 2568–2570.
40. M. Ding, X. Li, F. Wang, D. Shen, J. Wang, D. Tang, H. Zhu, Power scaling of diode-pumped Er:Y_2O_3 ceramic laser at 2.7 μm, Appl. Phys. Express 15 (2022) 062004.
41. W. Yao, H. Uehara, S. Tokita, H Chen, D Konishi, M Murakami, R Yasuhara, LD-pumped 2.8 μm Er:Lu_2O_3 ceramic laser with 6.7 W output power and >30% slope efficiency, Appl. Phys. Express 14 (2021) 012001.
42. A. Uvarova, P. Loiko, S. Kalusniak, E. Dunina, L. Fomicheva, A. Kornienko, S. Balabanov, A. Braud, P. Camy, C. Kränkel, Stimulated-emission cross-sections of trivalent erbium ions in the cubic sesquioxides Y_2O_3,Lu_2O_3, and Sc_2O_3, Opt. Mater. Express 13 (2023) 1385-1400.
43. M. Pollnau, T. Graf, J. E. Balmer, W. Lüthy, H. P. Weber, Explanation of the cw operation of the Er^{3+} 3-μm crystal laser, Phys. Rev. A 49 (1994) 3990.
44. J. B. Gruber, K. L. Nash, D. K. Sardar, U. V. Valiev, N. Ter-Gabrielyan, L. D. Merkle, Modeling optical transitions of Er^{3+} ($4f^{11}$) in C_2 and C_{3i} sites in polycrystalline Y_2O_3, J. Appl. Phys. 104 (2008).
45. R. Maksimov, V. Shitov, V. Osipov, O. Samatov, D. Vakalov, F. Malyavin, L. Basyrova, P. Loiko, P. Camy, Fabrication, microstructure and mid-infrared luminescence of Er:$(Sc_xY_{1-x})_2O_3$ transparent ceramics, Opt. Mater. 137 (2023) 113542.

46. R. D. Shannon, Revised effective ionic radii and systematic studies of interatomic distances in halides and chalcogenides, Found. Crystallogr. 32 (1976) 751-767.
47. F. Cassouret, A. Nady, P. Loiko, S. Normani, A. Braud, W. Chen, V. Petrov, D. Sun, P. Zhang, B. Viana, A. Hideur, Polarization switching in a mid-infrared Er:$YAlO_3$ laser, Opt. Lett. 49 (2024) 2970-2973.
48. P. Loiko, A. Volokitina, X. Mateos, E. Dunina, A. Kornienko, E. Vilejshikova, M. Aguiló, F. Diaz, Spectroscopy of Tb^{3+} ions in monoclinic $KLu(WO_4)_2$ crystal application of an intermediate configuration interaction theory, Opt. Mater. 78 (2018) 495-501.
49. A. A. Kornienko, A. A. Kaminskii, E. B. Dunina, Dependence of the line strength of *f–f* transitions on the manifold energy. II. Analysis of Pr^{3+} in $KPrP_4O_{12}$, Phys. Stat. Sol. (b) 157 (1990) 267-273.
50. D. E. Zelmon, J. M. Northridge, N. D. Haynes, D. Perlov, K. Petermann,, Temperature-dependent Sellmeier equations for rare-earth sesquioxides, Appl. Opt. 52 (2013) 3824-3828.
51. Y. Y. Yeung and P. A. Tanner, Trends in Atomic Parameters for Crystals and Free Ions across the Lanthanide Series: The Case of $LaCl_3$:Ln^{3+}, J. Phys. Chem. A 119 (2015) 6309-6316.
52. B. Aull, and H. Jenssen, Vibronic interactions in Nd:YAG resulting in nonreciprocity of absorption and stimulated emission cross sections, IEEE J. Quantum Electron. 18 (1982) 925-930.
53. S. A. Payne, L. L. Chase, L. K. Smith, W. L. Kway, W. F. Krupke, Infrared cross-section measurements for crystals doped with Er^{3+}, Tm^{3+} and Ho^{3+}, IEEE J. Quantum Electron. 28 (1992) 2619–2630.
54. J. B. Gruber, R. P. Leavitt, C. A. Morrison, N. C. Chang, Optical spectra, energy levels, and crystal-field analysis of tripositive rare-earth ions in Y_2O_3. IV. C_{3i} sites, J. Chem. Phys. 82 (1985) 5373-5378.
55. J. R. Dean and D. Bloor, Spectroscopy of rare earth oxide systems. II. Spectroscopic properties of erbium oxide (at antiferromagnetic transition), J. Phys. C: Solid State Phys. 5 (1972) 2921.
56. J. Blanusa, M. Mitric, D. Rodic, A. Szytula, M. Slaski, An X-ray diffraction and magnetic susceptibility study of $Tm_xY_{2-x}O_3$, J. Magn. Magn. Mater. 213 (2000) 75–81.
57. M. Mitric, B. Antic, M. Balanda, D. Rodic, M. L. Napijalo, An X-ray diffraction and magnetic susceptibility study of $Yb_xY_{2-x}O_3$, J. Condens. Matter Phys. 9 (1997) 4103–4111.